



# MoO<sub>2</sub>-C@MoS<sub>2</sub>: A unique cocatalyst with LSPR effect for enhanced quasi-full-spectrum photocatalytic hydrogen evolution of CdS

Yaoyao Li <sup>a,b</sup>, Chenfang Lou <sup>a,b</sup>, Wenlin Huang <sup>a</sup>, Ziqiang Ma <sup>a,b</sup>, Shukai Lin <sup>a</sup>, Xuelian Xie <sup>a</sup>, Tianhao He <sup>a</sup>, Xiaokang Lu <sup>a</sup>, Nairong Chen <sup>a,b</sup>, Jiandong Zhuang <sup>a,b,\*</sup>

<sup>a</sup> College of Materials Engineering, Fujian Agriculture and Forestry University, Fuzhou 350002, China

<sup>b</sup> National Forestry and Grassland Administration Key Laboratory of Plant Fiber Functional Materials, Fujian Agriculture and Forestry University, Fuzhou 350002, China



## ARTICLE INFO

**Keywords:**  
MoO<sub>2</sub>-C@MoS<sub>2</sub> cocatalyst  
LSPR effects  
Quasi-full-spectrum driven  
Photocatalytic hydrogen evolution  
CdS

## ABSTRACT

A well-designed cocatalyst structure can improve the light-harvesting and quantum efficiency of photocatalysis. A multidimensional MoO<sub>2</sub>-C@MoS<sub>2</sub> (MOCS) cocatalyst was successfully synthesized by post-sulfidation of MoO<sub>2</sub>-C nanorods. This controlled sulfidation process effectively inhibits the undesired oxidation of MoO<sub>2</sub>, stabilizing its metallicity and creating a synergistic effect for H<sub>2</sub> evolution. Firstly, the highly dispersed metallic MoO<sub>2</sub> nanoparticles induce localized surface plasmon resonance effects, expanding the light-harvesting range and generating abundant hot electrons. Secondly, the build-in electrostatic field and highly conductive carbon framework facilitates efficient interfacial electrons transfer. Thirdly, the amorphous MoO<sub>x</sub> and fragmented few-layers MoS<sub>2</sub> in MOCS provide dual active sites with superior intrinsic activity for H<sub>2</sub> evolution. Moreover, the unique multi-interface structure of MOCS optimizes the separation and reaction of charge carriers. As a result, the 20 wt% MOCS/CdS system show an excellent quasi-full-spectrum driven photocatalytic H<sub>2</sub> evolution activity of 48.41 mmol/h·g, with 4.03 mmol/h·g in near-infrared region (> 800 nm).

## 1. Introduction

Hydrogen (H<sub>2</sub>) is a clean, efficient, and versatile energy source that can be produced from a variety of sources, including renewable resources such as wind, solar, and hydroelectric power. Among them, photocatalytic H<sub>2</sub> production stands out as an ideal approach to generate H<sub>2</sub> fuel utilizing sunlight as the energy source [1–4]. Over the years, numerous novel photocatalysts driven by visible-light have been developed with the aim of maximizing the utilization and conversion of solar energy. Known for its narrow band gap and suitable conduction band potential, CdS is considered a favorable candidate for visible-light H<sub>2</sub>-evolution photocatalysis [5–7]. However, the practical application of single-component CdS photocatalyst is severely restricted due to its limited light response range (typically restricted to the ultraviolet or visible regions) and the low light quantum efficiency.

To develop a broad-spectrum photocatalyst with high efficiency, extensive research has focused on the construction of heterojunctions structures with a basal photocatalyst to improve charge carrier dynamics, light absorption properties and facilitate efficient photocatalysis [8]. For instance, by integrating CdS with suitable cocatalysts, it

becomes possible to harness a broader range of the solar spectrum and enhance the charge separation and transfer processes [9]. In recent years, Molybdenum-based cocatalysts have gained popularity as substitutes for scarce noble metals in photocatalytic hydrogen evolution due to their abundance, affordability, and adjustable electronic properties [10–12]. As a widely available and inexpensive metal oxide, MoO<sub>2</sub> has demonstrated significant potential in energy storage and catalysis [13–15]. More importantly, MoO<sub>2</sub> distinguishes itself from other intermediate valence metal oxides by its exceptional conductivity, resembling that of a quasi-metal [16]. This high conductivity ensures the presence of numerous free electrons within MoO<sub>2</sub>, a crucial requirement for initiating the localized surface plasmon resonance (LSPR) effect [17, 18]. The LSPR effect refers to the collective motions of the electrons triggered by light irradiation. When light of a specific wavelength interacts with the cocatalyst, it excites the surface plasmons, leading to a localized enhancement of the electromagnetic field. The adjustable resonance wavelength allows the plasmonic photocatalysts to efficiently harvest sunlight from the UV to near-infrared (NIR, over 40% of the solar spectrum) region. Additionally, the LSPR effect facilitates a process known as hot electron injection, which can greatly enhance the transfer

\* Corresponding author at: College of Materials Engineering, Fujian Agriculture and Forestry University, Fuzhou 350002, China.  
E-mail address: [jdzhuang@gmail.com](mailto:jdzhuang@gmail.com) (J. Zhuang).

and separation efficiency of photoexcited charge carriers [19].

The LSPR effect in cocatalyst is particularly advantageous for quasi-full-spectrum photocatalytic hydrogen evolution. However, current research on the LSPR effect of  $\text{MoO}_2$  nanoparticles (NPs) in the context of assisted quasi-full-spectrum photocatalytic  $\text{H}_2$ -evolution remains relatively limited. In our previous work [20],  $\text{MoO}_2\text{-C}$  (MOC,  $\text{MoO}_2$  nanoparticles embedded in carbon nanorods) was found to be an effective cocatalyst in the photocatalytic  $\text{H}_2$  evolution (PHE) process of  $\text{CdS}$ . However, the LSPR effect of MOC cocatalyst was weak, and there is still a great potential for improvement in its cocatalytic activity. One key factor contributing to the weak LSPR effect may be that the inevitability of  $\text{MoO}_2$  to oxidize into the semiconductor  $\text{MoO}_3$  when exposed to the atmosphere [21]. This transformation will deteriorate the conductivity as well as the LSPR effect of metallic  $\text{MoO}_2$ , and the same phenomenon has also been observed in other LSPR active metal oxides [18], such as  $\text{W}_{18}\text{O}_{49}$  and  $\text{Cu}_2\text{O}$ .

In order to stabilize  $\text{MoO}_2$  in its metallic state, an effective strategy is to use a controllable sulfurization process to form  $\text{MoS}_2$  on the surface of  $\text{MoO}_2$ . The sulfurization process offers multiple advantages in enhancing the properties of  $\text{MoO}_2$  nanoparticles. Firstly, it can effectively maintain the tetravalent state of Mo and inhibit the undesired oxidation of  $\text{MoO}_2$ . This preservation of the metallic state ensures optimal conductivity and electron transfer capabilities in catalytic applications. Additionally, the introduced  $\text{MoS}_2$  can act as a superior cocatalyst for  $\text{H}_2$ -evolution reaction (HER) applications [22,23]. Due to its strong affinity with atomic hydrogen, the presence of  $\text{MoS}_2$  enhances the hydrogen adsorption, activation, and subsequent reactions, improving catalytic performance and overall efficiency [24]. This strategic approach can simultaneously stabilize the metallicity of  $\text{MoO}_2$  and introduce  $\text{MoS}_2$  as a highly active hydrogen desorption species, resulting in a high-performance Mo-based  $\text{H}_2$ -evolution cocatalysts with LSPR effect.

In this work, a facile method was utilized to obtain high-performance  $\text{MoO}_2\text{-C}@\text{MoS}_2$  (MOCS) cocatalyst with LSPR effect, which was then employed to boost the photocatalytic hydrogen evolution performance of  $\text{CdS}$  (as shown in Scheme 1). The MOCS cocatalyst consists of numerous highly-dispersed  $\text{MoO}_2$  nanoparticles (NPs) embedded in carbon nanorods (NRs) matrix ( $\text{MoO}_2\text{-C}$ ) as cores, and few-layers  $\text{MoS}_2$  nanosheets (NSs) as wings grown on  $\text{MoO}_2$  surface. The metallic  $\text{MoO}_2$  NPs can induce electron accumulation to generate the LSPR effect, which can not only expand the photocatalyst's light harvest range to the near-infrared region, but also excite "hot electrons" injection process to promote charges transfer. Moreover, the combination of conductive  $\text{MoO}_2$  NPs and carbon NRs creates favorable conditions for rapid interfacial charge transfer, while the inclusion of  $\text{MoO}_x$  and few-layers  $\text{MoS}_2$  provides a multitude of active sites with superior intrinsic

activity for HER. As a result, the MOCS/ $\text{CdS}$  composite exhibits an outstanding quasi-full-spectrum PHE activity under light irradiation. The developed broad-spectrum MOCS/ $\text{CdS}$  photocatalysts with high quantum efficiency holds immense potential for various applications, including renewable energy generation and environmental remediation.

## 2. Experimental

### 2.1. Catalyst preparation

#### 2.1.1. Materials

All reagents used in the present work were of analytical grade and used without further treatment. Ultrapure water (resistivity  $> 18 \text{ M}\Omega \text{ cm}$ ) was used in all the experiments.

#### 2.1.2. Synthesis of the $\text{CdS}$ nanorods

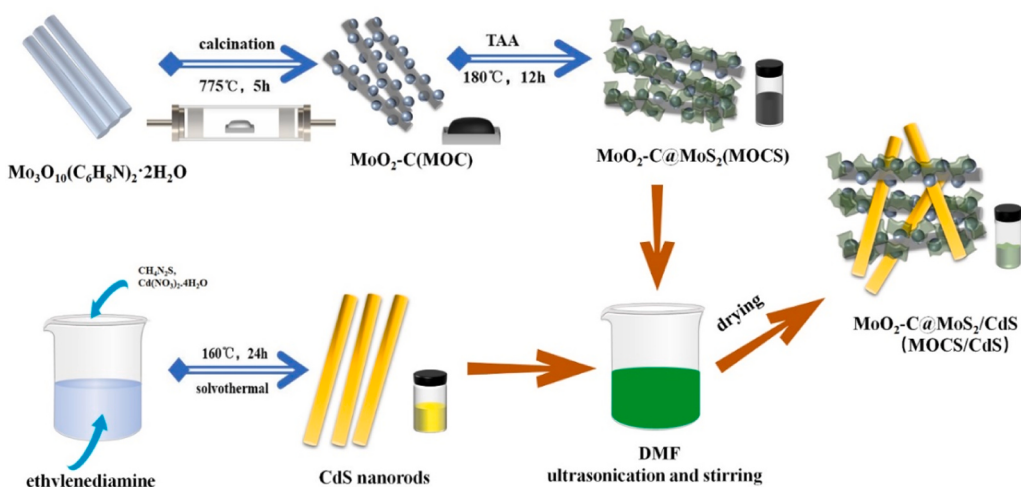
Typically, cadmium nitrate tetrahydrate (0.02 mol) and thiourea (0.06 mol) were dissolved into 60 mL ethylenediamine under continuous stirring. After about 30 min stirring, the homogenous mixture was transferred into a 100 mL Teflon lined stainless steel autoclave, and held at 160 °C for 50 h. After cooling down to the room temperature, the precipitates were gathered by centrifugation and washed with absolute ethanol and water, then dried at 50 °C overnight. The one-dimension  $\text{CdS}$  nanorods were finally obtained.

#### 2.1.3. Synthesis of the $\text{MoO}_2\text{-C}$ cocatalyst

The  $\text{MoO}_2\text{-C}$  (MOC) intermediate was synthesized by calcining self-sacrificial template precursor  $\text{Mo}_3\text{O}_{10}(\text{C}_6\text{H}_8\text{N})_2\cdot 2\text{H}_2\text{O}$ . Add 2.5 g ammonium molybdate tetrahydrate and 3.3 mL aniline to 40 mL pure water for full dissolution. Then 2 M hydrochloric acid was added slowly drop by drop to adjust the PH of the solution to 4.5. After the solution was reacted at 50 °C for 3 h, the product ( $\text{Mo}_3\text{O}_{10}(\text{C}_6\text{H}_8\text{N})_2\cdot 2\text{H}_2\text{O}$ ) was filtered and washed repeatedly with ethanol and dried for 6 h. The MOC cocatalyst was prepared by calcination of the dried precursor at 775 °C for 5 h at an increasing rate of 5 °C/min in a flowing  $\text{N}_2$  atmosphere (100 mL/min) [20].

#### 2.1.4. Synthesis of the $\text{MoO}_2\text{-C}@\text{MoS}_2$ cocatalyst

The  $\text{MoO}_2\text{-C}@\text{MoS}_2$  (MOCS) cocatalyst was obtained by sulfurizing MOC. Dissolved 240 mg MOC and 80 mg thioacetamide in a hydrothermal kettle liner containing 40 mL deionized water. After the ultrasonic waves were dispersed for 30 min, the solution that has been ultrasonicated were placed in a 100 mL Teflon-lined stainless-steel autoclave and heated at 180 °C for 12 h. After cooling to room temperature, washed the black product with water and ethanol alternately 3



Scheme 1. Scheme illustration of the preparation process of the MOCS/CdS hybrid photocatalyst.

times. Dried in a 60 °C vacuum drying oven for 24 h and collected for using.

#### 2.1.5. Synthesis of the $\text{MoO}_2\text{-C@MoS}_2\text{/CdS}$ composites

To prepare the MOCS/CdS composite, 100 mg of CdS nanorods and 20 mg of MOCS cocatalyst were mixed in 10 mL of  $\text{HCON}(\text{CH}_3)_2$  (DMF) and stirred for 12 h. The resulting mixture was then dried in an oven at 60 °C for 12 h, resulting in the formation of a composite with a lime-green color, consisting of  $\text{MoO}_2\text{-C@MoS}_2\text{/CdS}$ . In addition, MOCS/CdS composites containing 10 wt% (5 mg) and 30 wt% (15 mg) MOCS were also prepared under the same conditions.

#### 2.2. Characterizations

The products were characterized using multiple analytical techniques. X-ray diffraction (XRD) patterns were recorded on a Bruker D8 X-ray diffractometer using  $\text{CuK}\alpha$  radiation at 40 kV and 0.04 Å. X-ray photoelectron spectra (XPS) and UV photoelectron spectra (UPS) characterizations were determined by a Thermo ESCALAB 250 photoelectron spectrometer system. Field-emission scanning electron microscopy (FESEM) investigations were performed on a Hitachi SU-8010 microscope, while transmission electron microscopy (TEM and HR-TEM) images were captured by a FEI Tecnai G2F20 S-TWIN with a 200 kV accelerating voltage. Nitrogen sorption isotherms at 77 K were measured on a Micromeritics ASAP 2460 system. The optical absorption properties of the samples were analyzed using the ultraviolet-visible diffuse reflectance spectroscopy (UV-vis DRS) with  $\text{BaSO}_4$  as the background in a Lambda 750, PerkinElmer UV-vis spectrophotometer. The time-resolved photoluminescence (TRPL) spectra were obtained using a FLS1000 (Edinburgh Instruments), an excitation using 300 nm light source and monitoring of lifetime at 470 nm. The photoluminescence (PL) spectra were obtained using a Varian Cary-Eclipse 500 with an excitation wave-length at 300 nm. The photoelectric properties of the samples were investigated with conventional three-electrode cell and a ZENNIMUM electrochemical workstation (Zahner, Germany). A 10 mg catalyst sample and 20  $\mu\text{L}$  Nafion reagent were ultrasonicated in 0.5 mL DMF to get a slurry, which was then evenly deposited onto a 0.5 cm × 0.5 cm window of FTO conducting glass to serve as the working electrode, while the Ag/AgCl electrode as the reference electrode and Pt as the counter electrode. For photocurrent tests, a 0.2 M  $\text{Na}_2\text{SO}_4$  aqueous solution was used as the electrolyte, accompanied by a 300 W Xe-lamp with a cutoff filter ( $\lambda \geq 420$  nm). The electrochemical impedance spectroscopy (EIS) tests were carried out using a  $\text{K}_3[\text{Fe}(\text{CN})_6]/\text{K}_4[\text{Fe}(\text{CN})_6]/\text{KCl}$  aqueous solution as the electrolyte.

#### 2.3. Photocatalytic activity

The photocatalytic hydrogen evolution performance of MOCS/CdS composites was evaluated in an online photocatalytic hydrogen production system (Lab Solar 6 A, Perfect Light Co.). The process requires cooling water and a vacuum. Typically, ultrasonic dispersion of 25 mg catalyst sample in 50 mL 10 vol% lactic acid solution (as hole sacrificial agent), A 300 W xenon lamp with cutoff filters ( $420 \text{ nm} < \lambda < 800 \text{ nm}$ ,  $\lambda > 800 \text{ nm}$ ) were used as light sources to irradiate the reaction vessel vertically to generate  $\text{H}_2$ . The reaction vessel is degassed and then kept at 4 °C by recirculating the cooling system. Hydrogen was detected every hour by online gas chromatography (GC7806) using argon as carrier gas. The apparent quantum efficiency (AQE) at 450 nm was determined under the same reaction condition with irradiation using 450 nm narrow band pass filter. The AQE was calculated using the following formula [25]:

$$AQE = \frac{2 \times \text{number of evolved } \text{H}_2 \text{ molecules}}{\text{number of incident photons}} \times 100\%$$

### 3. Results and discussion

#### 3.1. Phase composition and morphology analyses

As shown in Fig. 1, the XRD diffraction patterns of the pure CdS can be perfectly indexed to the wurtzite structure of hexagonal CdS (JCPDS No.77-2306), while that of the MOC cocatalyst matches well with the standard monoclinic  $\text{MoO}_2$  (JCPDS No.73-1249). After sulfurization, the peak intensity of  $\text{MoO}_2$  in the MOCS cocatalyst significantly decreased, but interestingly, no identifiable diffraction peaks corresponding to  $\text{MoS}_2$  can be observed in the patterns. This outcome demonstrates that the sulfurization process of  $\text{MoO}_2$  was effectively executed, and the obtained  $\text{MoS}_2$  may exist in a non-aggregated form that cannot be detected by XRD. The XRD patterns of MOCS/CdS reveal that MOCS decoration has no obvious effect on the wurtzite structure of CdS, while a new minor diffraction peak (26.12°) corresponding to the (011) lattice plane of  $\text{MoO}_2$  can be observed. The presence of this low-intensity diffraction peak indicates the successful combination of MOCS and CdS [26], as it results from the overlapping of their respective diffraction peaks at 26.08° and 26.53°.

The morphology and microstructure of MOC, MOCS and MOCS/CdS composites were characterized by FESEM and TEM images. As depicted in Fig. 2a, the MOC sample obtained by the heat treatment of  $\text{Mo}_3\text{O}_10$  ( $\text{C}_6\text{H}_8\text{N}_2\text{O}_2\text{H}_2\text{O}$ ) is comprised of 1D carbon NRs and numerous irregular  $\text{MoO}_2$  NPs with an average diameter of ~50 nm. In addition, these  $\text{MoO}_2$  NPs are firmly embedded within the carbon framework, ensuring their high dispersion throughout the post-treatment process and subsequent catalytic applications. More importantly, considering the metallicity of  $\text{MoO}_2$ , these highly dispersed nanoparticles may serve as sensitive emitters for LSPR effect. After post-sulfurization (Fig. 2b), wing shaped 2D  $\text{MoS}_2$  NSs grow vertically on the surface of  $\text{MoO}_2$  NPs, while the overall rod-shape frameworks are well retained. The TEM image shown in Fig. 2c also demonstrates the 0-D  $\text{MoO}_2$  NPs, 1-D amorphous carbon NRs, and 2-D  $\text{MoS}_2$  NSs seamlessly grow together to form a cohesive structure with rod-shaped morphology. It is worth noting that the nano-size of the  $\text{MoO}_2$  NPs allows for the control and restriction of the width of the grown  $\text{MoS}_2$  NSs. As the catalytic function of  $\text{MoS}_2$  is primarily attributed to its edge atoms, these highly dispersed fragmented  $\text{MoS}_2$  NSs with limited width can not only offer abundant active edge sites, but also enhance the intrinsic activity of active sites for hydrogen evolution reaction. Moreover, the BET specific surface areas (Fig. S1) of MOCS and MOC cocatalysts are measured to be 38.93  $\text{m}^2/\text{g}$  and 6.14  $\text{m}^2/\text{g}$ , respectively, indicating that the sulfurization process can endow cocatalyst with a higher specific surface area and subsequently more active sites.

The ternary hybrid intimate heterostructure of  $\text{MoO}_2\text{-C@MoS}_2$  can be further confirmed by the corresponding HR-TEM images. As shown in

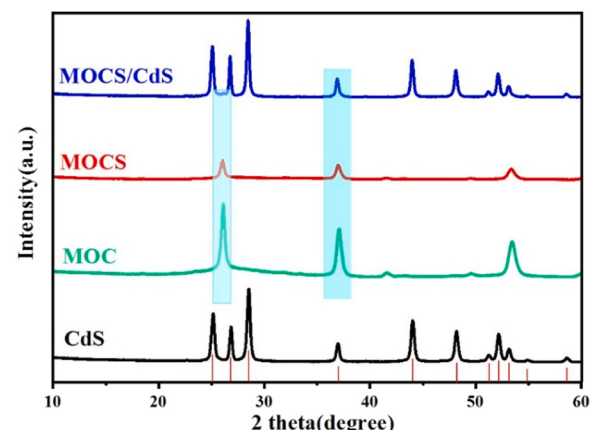
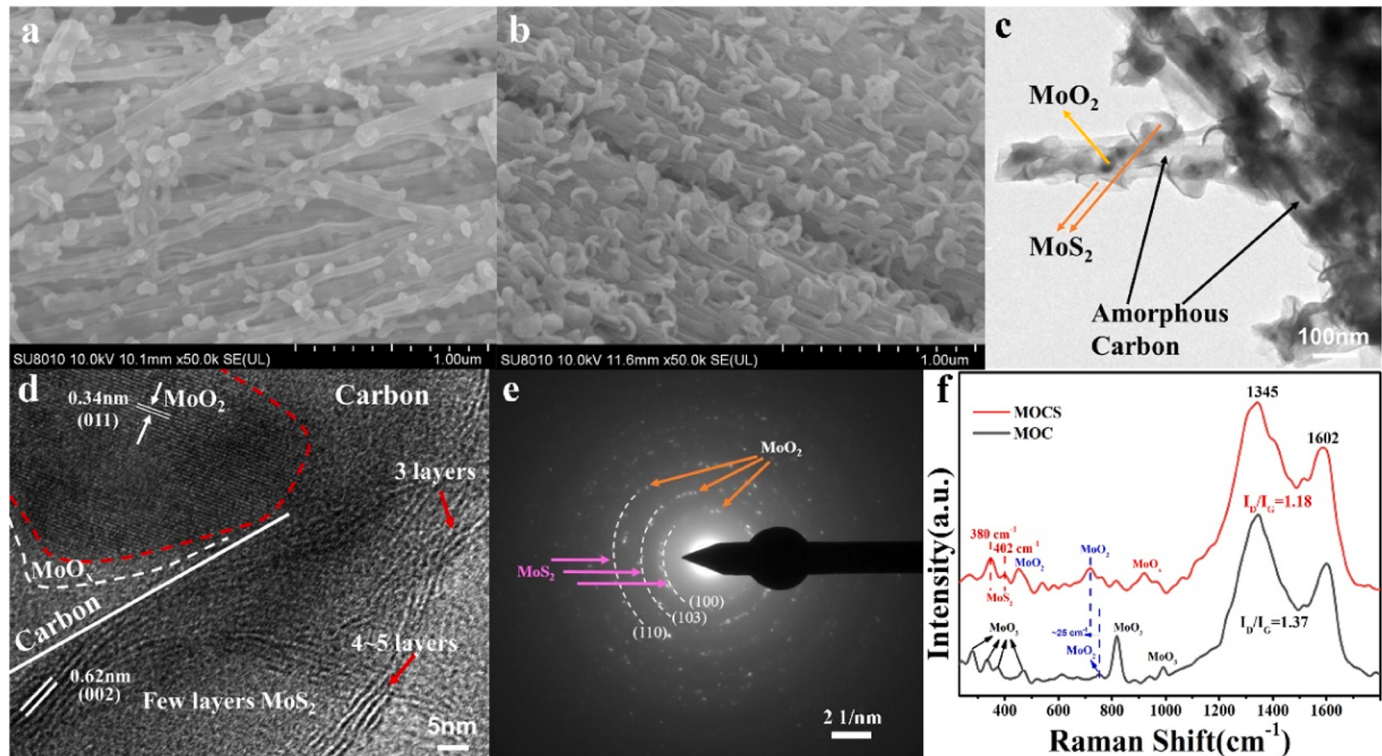


Fig. 1. XRD patterns of CdS, MOC, MOCS and MOCS/CdS.



**Fig. 2.** (a) SEM image of MOC nanorods, (b) SEM image, (c) TEM image, (d) HRTEM image and (e) SAED image of MOCS nanorods, and (f) Raman spectra of MOC and MOCS.

**Fig. 2d**, the MoO<sub>2</sub> NPs with characteristic (011) plane spacing of 0.34 nm is embedded in amorphous carbon materials. As expected, there is a disordered interface region (MoO<sub>x</sub>) formed at the interface between the MoO<sub>2</sub> NPs and amorphous carbon, implying a unique interface microstructure with good interfacial bonding [27]. In previous studies [20,28], the MoO<sub>x</sub> species have been proved can act as effective active sites to trap photoelectrons and activate the adsorbed water molecules in the photocatalytic water splitting. Note that there are some irregular lamellar substances riveting intimately on MoO<sub>2</sub> NPs, and the interlayer spacing of ~0.62 nm can be assigned to the 2D MoS<sub>2</sub>. In addition, the lamellar MoS<sub>2</sub> NSs obtained through the sulfurization treatment of MoO<sub>2</sub> NPs have the structural characteristics of few-layers (3–5 layers), which can provide more active edge sites for HER than MOC cocatalyst and stacked MoS<sub>2</sub> [29]. The SAED pattern of MOCS shown in **Fig. 2e** also exhibits two distinct sets of diffraction rings, which can be well assigned to the (110), (210), and (312) planes of MoO<sub>2</sub> as well as the (100), (103), and (110) planes of MoS<sub>2</sub>, respectively [30].

In **Fig. 2f**, Raman spectra of MOC and MOCS are provided to analyze the impact of sulfurization on the structure of C, MoO<sub>2</sub> and MoS<sub>2</sub> components and their interaction. As depicted, the D peak at around 1350 cm<sup>-1</sup> is generated by lattice defects and partial disordered structures in graphite [31], while the G peak at around 1600 cm<sup>-1</sup> represents the E<sub>2g</sub> vibration mode of sp<sup>2</sup> hybridized carbon rings in primary scattering [32]. Their intensity ratio (I<sub>D</sub>/I<sub>G</sub>) reflects the defect degree of carbon materials. The MOCS shows a lower I<sub>D</sub>/I<sub>G</sub> value (1.18) compared to MOC (1.37), revealing the sulfurization process can reduce the defect degree of carbon components [33], enhance their conductivity and promote the effective migration of electrons in the cocatalyst. The MOC Raman spectrum also exhibits prominent peaks at around 280 cm<sup>-1</sup>, 334 cm<sup>-1</sup>, 374 cm<sup>-1</sup>, 469 cm<sup>-1</sup>, 818 cm<sup>-1</sup>, and 990 cm<sup>-1</sup>, which are distinctive characteristics of MoO<sub>3</sub> [34,35]. In addition, a peak at around 746 cm<sup>-1</sup> is observed, indicating the presence of MoO<sub>2</sub>. This result suggests that the MOC contains a substantial amount of MoO<sub>3</sub>, primarily resulting from the oxidation of the MoO<sub>2</sub> NPs. This undesired

surface oxidation effect will lead to a deterioration in the metallic properties of MoO<sub>2</sub>. After sulfurization, the Raman spectra of MOCS no longer exhibit the characteristic peaks of MoO<sub>3</sub>, except for a weak peak at 818 cm<sup>-1</sup>. Instead, some new peaks emerge at around 380 cm<sup>-1</sup>, 402 cm<sup>-1</sup>, 452 cm<sup>-1</sup>, 721 cm<sup>-1</sup>, and 916 cm<sup>-1</sup>. Among these, the peaks at 380 cm<sup>-1</sup> and 402 cm<sup>-1</sup> is related to the E<sub>2g</sub><sup>1</sup> and A<sub>1g</sub> vibration mode of interlayer hexagonal MoS<sub>2</sub> [36,37], confirming the successful sulfurization of MoO<sub>2</sub> into MoS<sub>2</sub>. Moreover, the peak at 916 belongs to the vibrational mode of Mo-O bond in MoO<sub>3-x</sub> [38–41], while two strong peaks at 452 cm<sup>-1</sup> and 721 cm<sup>-1</sup> suggest a significant amount of MoO<sub>2</sub> in the sample [34]. It is worth noting that the peak position of MoO<sub>2</sub> in MOCS (721 cm<sup>-1</sup>) displays an obvious shift from its position in MOC (746 cm<sup>-1</sup>), indicating the strong interfacial interaction between MoO<sub>2</sub> and MoS<sub>2</sub> [42].

By integrating MOCS and CdS in DMF, the MOCS/CdS hybrid (as shown in **Fig. 3a**) retains its characteristic rod-like structure, comprising CdS NRs with concrete-like MOCS surface attachments. It is noteworthy that in the presence of DMF, the rod-like carbon framework exhibits a tendency to melt, behaving like a "cement" that securely binds (C-S) the MOCS cocatalyst to the CdS NRs, as illustrated in **Fig. 3b**. Further examination of the interfacial microstructure in **Fig. 3c** showed that the MoS<sub>2</sub> NSs could directly attach to the CdS NRs to form a heterojunction, and the amorphous carbon and MoO<sub>2</sub> NPs can be found in the intergranular spaces. Overall, the MOCS/CdS hybrid exhibited a unique microstructure that allowed for efficient charge separation and transfer, making it a promising candidate for various photocatalytic applications.

### 3.2. Surface chemical environment analyses

The surface chemical states of the prepared samples were further analyzed by X-ray photoelectron spectroscopy (XPS). The XPS survey spectra displayed in **Fig. S2** provide clear evidence of the presence of corresponding elements in each sample. To minimize surface charge effects, the C 1 s peak of neutral carbon (284.6 eV) was set as the

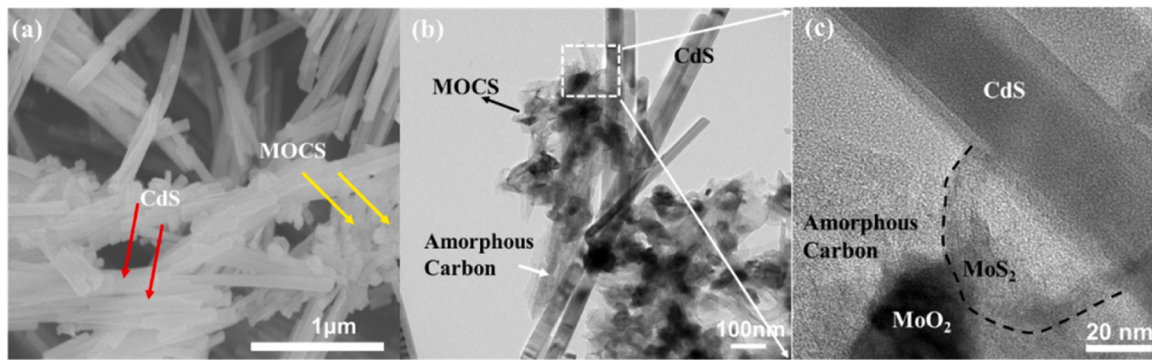


Fig. 3. (a) SEM and (b, c) TEM images of MOCS/CdS nanocomposites.

reference for all high-resolution spectra of elements. As shown in Fig. 4a, the C 1 s spectra of MOC and MOCS can be deconvoluted into three and four dominating peaks, respectively. In comparison to MOC, the intensity of the C-O peak in MOCS significantly decreases and a new peak emerges at 286.0 eV, indicating the transformation of C-O bonds into C-S bonds during the sulfurization process.

The high-resolution Mo 3d spectra presented in Fig. 4b reveal notable changes in the chemical states of Mo ions due to sulfurization. Within the range of 227–240 eV, the Mo 3d spectrum of MOC reveals three distinct sets of peaks, suggesting the simultaneous existence of three oxidation states of Mo ions ( $\text{Mo}^{6+}$ ,  $\text{Mo}^{4+}$  and  $\text{Mo}^{3+}$ ) [43–45]. The dominant  $\text{Mo}^{6+}$  signal peaks suggest extensive oxidation of  $\text{MoO}_2$  into  $\text{MoO}_3$  under atmospheric conditions, which is in good agreement with the Raman results shown in Fig. 2f. Notably, the presence of  $\text{Mo}^{3+}$  ions ( $3\text{d}_{5/2}$ , 229.18 eV and  $3\text{d}_{3/2}$ , 230.6 eV) resulting from carbon reduction

[20,46] offers further evidence for the formation of mixed-valence  $\text{MoO}_x$ . The formed  $\text{MoO}_x$  appears as a disordered region located at the interface of  $\text{MoO}_2$  NPs and carbon NRs in TEM image (Fig. 2d), and serves as an active site for trapping photoelectrons and activating adsorbed water molecules in the process of HER [47]. After sulfurization, the characteristic peaks corresponding to  $\text{Mo}^{6+}$  vanish, indicating that sulfurization process effectively hinders the undesired oxidation of  $\text{MoO}_2$ . Furthermore, the persistent characteristic peaks of  $\text{Mo}^{3+}$  and  $\text{Mo}^{4+}$  imply that sulfurization exclusively occurs on the surface of  $\text{MoO}_2$  NPs without affecting the presence of  $\text{MoO}_x$  at the  $\text{MoO}_2$ -C interface. In the MOCS/CdS composites, it is found that the relative intensity of the Mo 3d peaks decreased, but no new peaks or noticeable shifts in the peak positions have been identified as compared to MOCS. This indicates MOCS has excellent stability and will not undergo valence changes during the composite process with CdS.

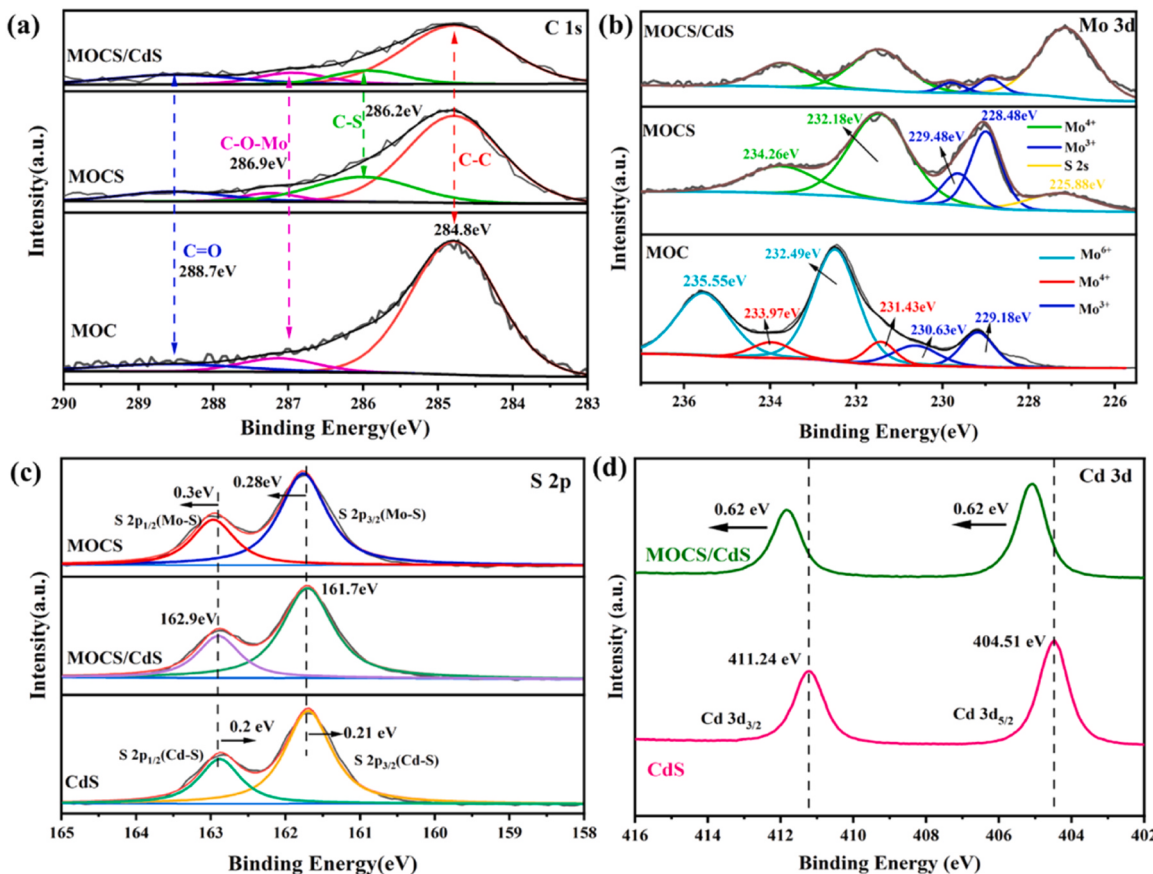


Fig. 4. High-resolution (a) C 1s, (b) Mo 3d, (c) S 2p and (d) Cd 3d XPS spectra of MOC, MOCS, CdS and MOCS/CdS.

The binding states of S element can be determined by analyzing the S 2p XPS signals. In Fig. 4c, it is found that the S 2p peaks in the MOCS/CdS composite are positioned between those in CdS and MOCS, indicating a successful combination of the two materials. Furthermore, due to the superior electron affinity of Mo over Cd, the S 2p signal peaks corresponding to the Mo-S bond of MoS<sub>2</sub> in MOCS experience a shift of ~0.5 eV to the higher binding energy compared to those in CdS (Cd-S bond). The observed peak shifts in the Cd 3d signal further confirm the above deduction (Fig. 4d). In comparison to CdS, the remarkable high-energy shift (~0.62 eV) of Cd 3d peaks in the MOCS/CdS composite signifies efficient binding between CdS and MoS<sub>2</sub>, with electrons tending to transfer from CdS to MOCS due to the higher electron affinity of Mo.

### 3.3. Photocatalytic H<sub>2</sub> evolution activity and stability

The photocatalytic H<sub>2</sub> evolution (PHE) performance of as-synthesized catalysts was evaluated under visible light (420 nm <  $\lambda$  < 800 nm) and NIR light ( $\lambda$  > 800 nm) irradiation using 10 vol% lactic acid as a sacrificial reactant. Fig. 5a shows the visible-light-driven H<sub>2</sub> evolution rate of MOCS/CdS hybrid photocatalysts with varying MOCS loading amounts, together with pristine CdS, and MOC and MOCS for comparison. MOC showed no obvious photocatalytic activity, while pristine CdS and MOCS showed H<sub>2</sub>-evolution rates of approximately 0.64 mmol/h·g and 0.42 mmol/h·g, respectively. The PHE performance of CdS can be significantly enhanced following the modification with MOCS. At a loading amount of 20 wt% MOCS, the optimized MOCS/CdS sample demonstrates a remarkable boost in PHE activity, resulting in a PHE rate of 43.06 mmol/h·g. This rate is approximately 67.3 times and 2.7 times that of pure CdS and MOC/CdS, respectively. In addition, to the best of our knowledge, the visible-light driven PHE performance of MOCS/CdS reported in this work is superior than most of those obtained by CdS decorated with Mo-based cocatalyst (Table S1).

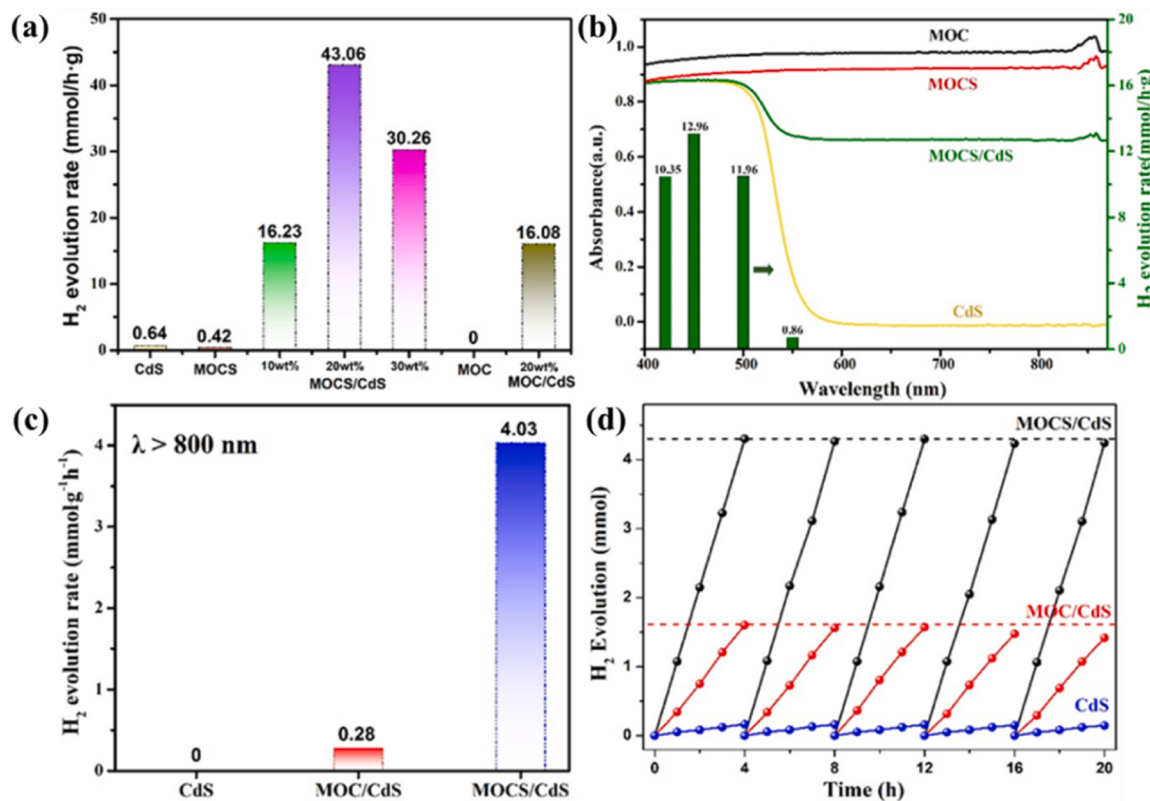


Fig. 5. (a) Visible light (420 nm <  $\lambda$  < 800 nm) driven PHE activities and (b) UV-vis DRS spectra of various samples and light-wavelength depended PHE performances of MOCS/CdS, (c) Photocatalytic activities of photocatalysts under NIR light irradiation ( $\lambda$  > 800 nm), and (d) Cycling test for the PHE performance of MOCS/CdS.

As evidenced in Fig. 5c, under the NIR light irradiation ( $\lambda > 800$  nm), the PHE rate of MOCS/CdS sample remains impressive at 4.03 mmol/h·g, surpassing that of the MOC/CdS sample (0.28 mmol/h·g) by over 14 times. The disparity in PHE activity between the MOCS/CdS and MOC/CdS samples is more pronounced in the NIR region than in the visible-light region, highlighting the superior LSPR effect of MOCS over MOC. This stark contrast in their LSPR effect primarily relies on the state of  $\text{MoO}_2$  NPs. The Raman and XPS analyses provide evidence that the  $\text{MoO}_2$  NPs in MOC are susceptible to oxidation, leading to the formation of semiconductor  $\text{MoO}_3$ , which restricts the LSPR effect of the MOC cocatalyst. It is worth noting that the sulfurization process can greatly enhance the oxidation resistance of metallic  $\text{MoO}_2$  NPs. As a result, the highly dispersed metallic  $\text{MoO}_2$  NPs can exist more stably within MOCS, and the synergistic effect of  $\text{MoO}_2$  NPs with other components ensures the effective release and utilization of their LSPR effect. Furthermore, when exposed to the full spectrum of a Xenon lamp (without filters), the MOCS/CdS sample exhibited an outstanding PHE activity of 48.41 mmol/h·g (Fig.S3), indicating excellent light response performance across the quasi-full spectrum.

In order to further assess the photocatalytic stability of CdS, MOC/CdS and MOCS/CdS, a continuous photocatalytic water splitting experiment were conducted for 20 h (total five cycles), and the results are compared in Fig. 5c. MOC/CdS demonstrates good stability during the initial three cycles, but its photocatalytic activity experienced a notable decline after 12 h of light irradiation. In contrast, the MOCS/CdS sample exhibited reproducible photocatalytic activity throughout all five cycles. Furthermore, comparing the XPS spectra (Fig. S4) of fresh and used MOCS/CdS photocatalysts reveals that the peak locations and intensities of C 1 s, Mo 3d, Cd 3d, and S 2 P core lines remained essentially unchanged, confirming its exceptional photostability as anticipated. Overall, the optical properties and PHE performance analyses demonstrate the improved light harvesting and enhanced photocatalytic activity of MOCS/CdS, highlighting its potential as a promising photocatalyst for efficient hydrogen evolution.

#### 3.4. Photoelectrochemical analyses

To determine the transfer direction of photogenerated electrons in the MOCS/CdS system, we analyzed the work functions ( $\Phi$ ) of CdS and MOCS using UPS characterization with a bias voltage of  $-5$  V. The work function can be obtained by examining the low kinetic energy cutoff ( $E_{\text{cutoff}}$ ) and the high kinetic energy cutoff ( $E_{\text{fermi}}$ ) of secondary electrons from the UPS spectrum with a specific photoenergy ( $\text{He I}$ ,  $h\nu = 21.22$  eV), using the formula  $\Phi = h\nu - |E_{\text{cutoff}} - E_{\text{fermi}}|$ . As shown in

Fig. 6a, the  $E_{\text{cutoff}}$  of CdS and MOCS are found to be 17.57 eV and 15.92 eV, respectively, while their  $E_{\text{fermi}}$  values are 3.54 eV and 2.79 eV, respectively. Therefore, the work functions ( $\Phi$ ) of CdS and MOCS are calculated to be 7.19 eV and 8.09 eV, respectively. Compared to CdS, MOCS exhibits a higher work function value and a lower Fermi energy level, which are mainly attributed to the presence of metallic  $\text{MoO}_2$  NPs and carbon NRs. This difference in work functions and Fermi level between CdS and MOCS results in the formation of build-in electrostatic field, facilitating the interfacial transfer of photoexcited electrons from CdS to MOCS and enhancing the separation efficiency of photogenerated charged carriers.

To elucidate the effective interfacial transfer of photogenerated charge carriers over MOCS/CdS composite, the time-resolved photoluminescence (TRPL) spectra of MOCS and MOCS/CdS were further measured. As depicted in Fig. 6b, by fitting the TRPL spectra of MOCS and MOCS/CdS with a biexponential function, the results indicate that the short lifetime ( $\tau_1$ ) primarily contributed by the radiative pathway is 1.92 ns for MOCS and 0.24 ns for MOCS/CdS, while the long lifetime ( $\tau_2$ ) reflecting non-radiative processes is 17.26 ns for MOCS and 2.59 ns for MOCS/CdS, respectively. The average fluorescence lifetime ( $\tau_{\text{ave}}$ ) of MOCS and MOCS/CdS is calculated to be 6.47 ns and 0.25 ns, respectively. Obviously, the  $\tau_{\text{ave}}$  of MOCS/CdS is much shorter than that of MOCS, revealing an ultrafast interfacial charge transfer process over MOCS/CdS heterojunctions [49,50].

Transient photocurrent response, electrochemical impedance spectroscopy (EIS), Bode phase analysis and linear sweep voltammetry (LSV) were used to study the generation and migration ability of charged carriers in various photocatalysts. Fig. 7a illustrates the transient photocurrent responses of various samples under visible light illumination. It is evident that the photocurrent intensity of MOCS/CdS is significantly greater than that of pure CdS and MOCS. Notably, the pure CdS sample exhibits a fast decay rate of photocurrent when the light is turned off, suggesting a high rate of carrier recombination. In contrast, the photocurrent in the MOCS/CdS heterojunction experiences a noticeably slower decay rate, implying that the presence of the MOCS cocatalyst can effectively improve the separation rate of charged carrier and prolong the lifetime of photogenerated electrons.

The impact of the MOCS cocatalyst on the photogenerated electron lifetime is further studied through Bode phase analysis. As depicted in Fig. 7b, the MOCS/CdS heterojunction displays a significant shift of peak frequency towards the lower region compared to pure CdS. This shift implies a longer photogenerated electron lifespan in the heterojunction, as the frequency is inversely related to the electron lifespan. Obviously, the prolonged electron lifespan in the MOCS/CdS heterojunction

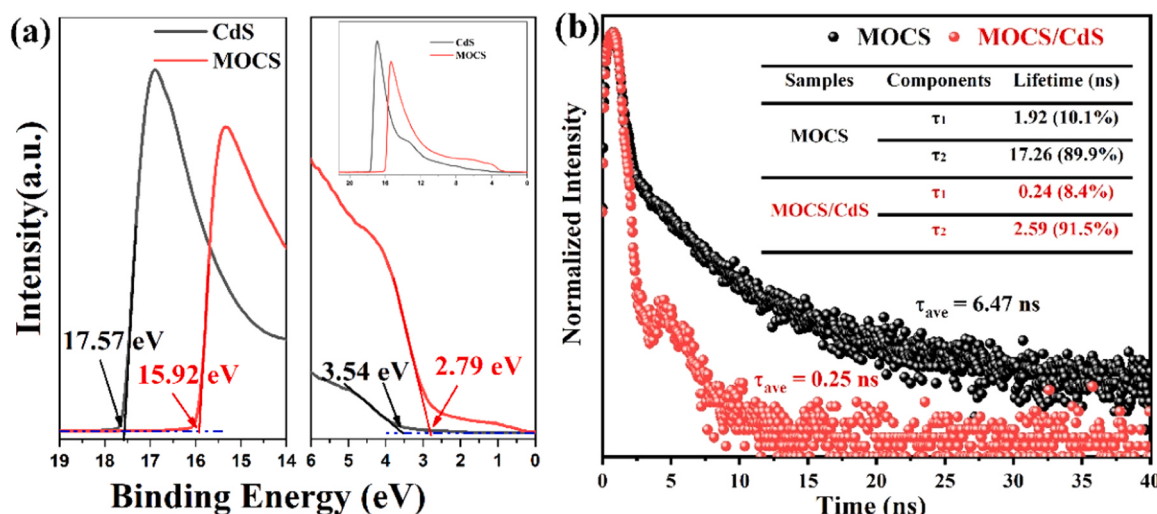
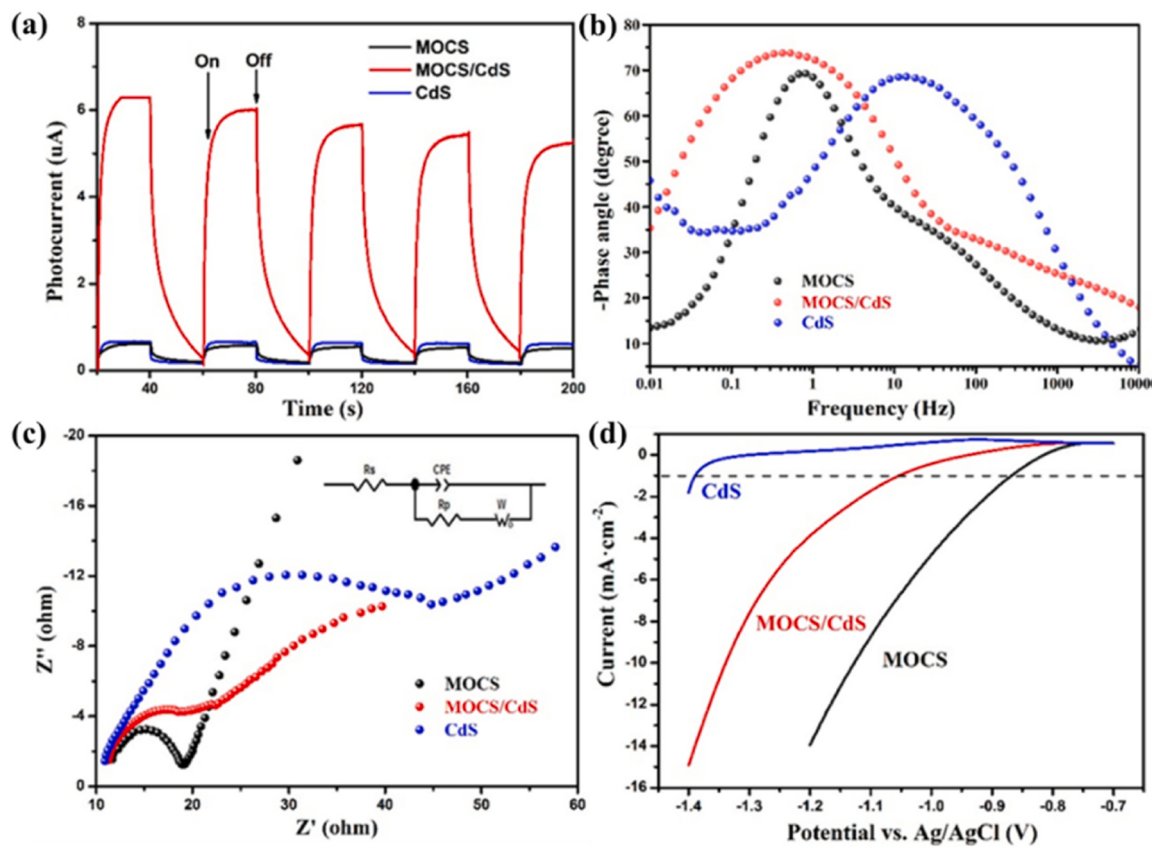


Fig. 6. (a) UPS spectra of CdS and MOCS, and (b) TRPL spectra of MOCS and MOCS/CdS.



**Fig. 7.** (a) Periodic photocurrent responses, (b) Nyquist impedance plots (with equivalent circuit), (c) Bode plots, and (d) polarization curves of CdS, MOCS and MOCS/CdS photocatalysts.

suggests that the MOCS cocatalyst can enhance the separation efficiency of photogenerated carriers and prolong the electron lifetime in the system. This inference can be further confirmed by the photoluminescence (PL) analysis. As shown in Fig. S5, the pure CdS sample exhibits a prominent PL peak at 525 nm (excitation  $\lambda = 380$  nm) due to its intrinsic exciton emission with a bandgap energy of 2.43 eV. In contrast, the PL strength of MOCS/CdS is significantly reduced compared to pure CdS. This reduction signifies that the MOCS cocatalyst can efficiently extract photogenerated electrons in CdS, thereby minimizing their recombination with holes.

EIS technique is a powerful tool for imploring the interfacial charge transfer ability and the charge recombination rate between different components. Fig. 7c shows a comparison of Nyquist plots using different electrodes. In all three samples, a capacitance arc is observed in the low frequency region, while the inclined line beyond the capacitance arc corresponds to the diffusion process in the electrolyte. In the EIS analysis, a smaller diameter semicircle arc represents an enhanced photogenerated charge transfer ability, which is responsible for high surface reaction kinetics [51]. The pure CdS sample exhibits a large diameter semicircular arc, suggesting a fast recombination rate of photogenerated charge carriers. On the other hand, the MOCS/CdS heterojunction shows a smaller diameter capacitance arc due to the efficient electron transfer from the CdS to the MOCS cocatalyst. Additionally, the MOCS cocatalyst electrode exhibits a semicircle of the smallest diameter, indicating its high conductivity.

In addition to the Nyquist plot analysis, an equivalent circuit model (Fig. 7c inset), including ohmic series resistance ( $R_s$ ), electron transfer resistance ( $R_p$ ), constant phase element (CPE), and Warburg resistance ( $W$ ), is employed to further understand the charge transfer behavior in the system. The obtained parameters are compared in Table 1 by fitting the Nyquist plots with this circuit model.  $R_p$  and  $W_R$  represent the

**Table 1**  
The equivalent circuit parameters after fitting.

Sample	$R_s$ ( $\Omega$ )	$R_p$ ( $\Omega$ )	$CPE \cdot T$ ( $F \cdot cm^{-2} \cdot s$ )	$W_R$ ( $\Omega$ )
CdS	10.26	44.45	$1.8 \times 10^{-4}$	103.3
MOC	8.56	15.55	$10.8 \times 10^{-4}$	110.6
MOCS	7.87	15.05	$7.3 \times 10^{-4}$	5.94
MOCS/CdS	10.39	21.48	$4.1 \times 10^{-4}$	46.08

$R_s$ : series resistance, here means solution resistance.

$R_p$ : parallel resistance, here means charge transfer resistance.

CPE: double-layer capacitance.

$W_R$ : resistance of Warburg element, here means material diffusion resistance.

charge transfer resistance and diffusion resistance at the electrochemical interface, respectively. The significantly lower  $R_p$  and  $W_R$  observed for MOCS indicates its high conductivity and surface activation. For MOC catalysts, the relatively high  $R_p$  indicates that surface oxidation of  $MoO_2$  would negatively impact conductivity and increase interfacial charge transfer resistance, while the extremely high  $W_R$  also indicates that surface oxidation reduces the surface reaction activity of MOC. Interestingly, for MOCS/CdS, there is a pronounced reduction in  $R_p$  and  $W_R$  resistance, suggesting improved mobility and reactivity of photogenerated charge carriers compared to pure CdS. Another significant distinction between CdS and MOCS/CdS is found in the CPE value. The capacitance value of CdS is derived from the double-layer capacitance, whereas the relatively much larger capacitance values of MOC and MOCS cocatalysts may originate from the formation of “electron trap”  $MoO_x$  at the interface, which serves as an electron storage repository [52]. In addition, the relatively large capacitance value of MOCS/CdS confirms the presence of numerous “electron trap zones” in the composites.

The electrochemical hydrogen evolution activities of CdS, MOCS,

and MOCS/CdS were compared using the linear sweep voltammetry (LSV) technique. The overpotential (the external driving potential required under a rated current density), an important index for evaluating electrochemical catalytic performances, is used to assess the difficulty of HER. By comparing the polarization curves depicted in Fig. 7d, it is found that pristine CdS exhibits a very low cathodic current density even under a high applied voltage. At the current density of  $1 \text{ mA}\cdot\text{cm}^{-2}$ , the overpotential of pristine CdS is measured to be  $-1.39 \text{ V}$ , reflecting a deficiency in HER activity. In contrast, both MOCS ( $-0.87 \text{ V}$ ) and MOCS/CdS ( $-1.05 \text{ V}$ ) show enhanced HER activities. This result highlights the exceptional performance of MOCS as a cocatalyst for  $\text{H}_2$  evolution, and it can effectively reduce the overpotential of the CdS semiconductor.

Obviously, these findings corroborate the beneficial effect of the MOCS cocatalyst on the photoelectrochemical properties of the MOCS/CdS composites. Firstly, the high-conductivity components ( $\text{MoO}_2$  NPs and carbon NRs) in MOCS can induce the LSPR effect, enhance the light-harvesting and electron transfer capabilities of the composites, resulting in improved generation, separation, and utilization of photogenerated charge carriers. Secondly, the formation of  $\text{MoO}_x$  at the interface between  $\text{MoO}_2$  NPs and carbon NRs can serve as a storage repository of electrons, thereby prolonging their lifespan. Thirdly, the presence of high intrinsic activity components in MOCS, such as  $\text{MoO}_x$  and few-layers  $\text{MoS}_2$ , provide dual active sites for HER. Finally, the multidimensional MOCS cocatalyst can decrease the mass diffusion resistance and  $\text{H}_2$ -evolution overpotential of CdS, further improving the reaction kinetics performance of the MOCS/CdS composite.

### 3.5. Mechanism of the synergistic effect of interfacial microstructure and components

Based on the aforementioned analysis, a preliminary hypothesis is put forth to explain the promoting mechanism of MOCS on the full-spectrum-driven PHE performance of the composited MOCS/CdS photocatalyst. Upon exposure to visible light, the primary photocatalyst CdS is stimulated, generating both holes ( $\text{h}^+$ ) and electrons ( $\text{e}^-$ ). Due to the disparate work functions of CdS and MOCS, a built-in electrostatic field is created at their interface, which accelerates the transfer of photogenerated  $\text{e}^-$  from CdS to MOCS, thereby increasing the separation efficiency of photogenerated charge carriers. Furthermore, the highly dispersed metallic  $\text{MoO}_2$  NPs are capable of harvesting NIR light through the LSPR effect, leading to the production of numerous "hot electrons". Thanks to the intimate bonding heterostructure and conductive carbon framework in MOCS, these excited electrons (photogenerated  $\text{e}^-$  and hot electrons) can swiftly migrate to active sites, such

as fragmented few-layers  $\text{MoS}_2$  and amorphous  $\text{MoO}_x$ , where they reduce protons to produce  $\text{H}_2$ . Meanwhile, the  $\text{h}^+$  remaining in the valence band of CdS participates in the reforming reaction of lactic acid. The intimate heterojunction, highly conductive components, and dual active sites work in tandem, enabling more efficient utilization of a broader range of the solar spectrum and promoting the separation and reaction of charge carriers, resulting in an excellent hydrogen evolution rate under quasi-full-spectrum illumination.

## 4. Conclusion

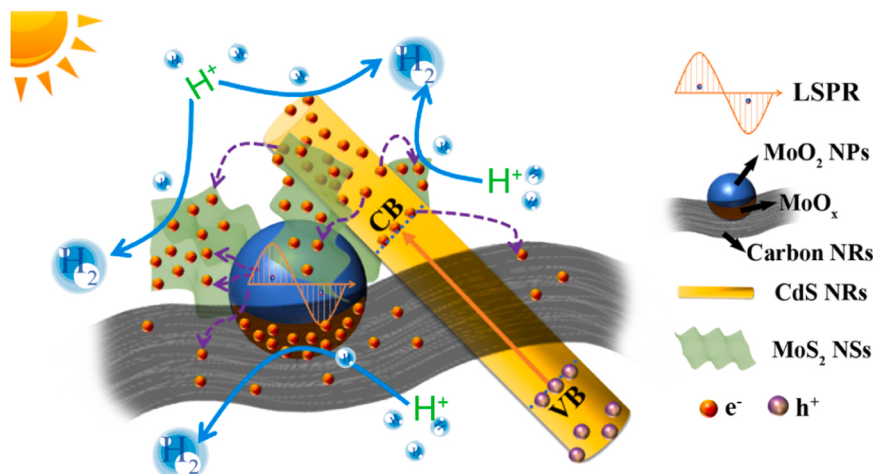
In conclusion, the successful synthesis of multidimensional MOCS cocatalysts via post-sulfidation of  $\text{MoO}_2$ -C nanorods effectively inhibits the undesired oxidation of  $\text{MoO}_2$  NPs. The highly dispersed metallic  $\text{MoO}_2$  NPs induce electron accumulation and generate LSPR effect, which extends the light absorption range of the photocatalyst to the NIR region. Additionally, the integration of conductive components ( $\text{MoO}_2$  NPs and carbon framework) and dual HER active components ( $\text{MoO}_x$  and few-layers  $\text{MoS}_2$ ) in this strategic approach creates a highly favorable environment for efficient charge transfer and abundant active sites. Therefore, the combination of MOCS cocatalysts with CdS significantly improves the separation efficiency of photo-generated electron-hole pairs in CdS, prolongs the lifetime of charge carriers, reduces the hydrogen evolution overpotential, and demonstrates exceptional quasi-full-spectrum photocatalytic performance in hydrogen production. As a result, the 20 wt% MOCS/CdS system exhibits excellent PHE activity, with rates of  $43.06 \text{ mmol}/\text{h}\cdot\text{g}$  in the visible light region ( $420 \text{ nm} \sim 800 \text{ nm}$ ),  $4.03 \text{ mmol}/\text{h}\cdot\text{g}$  in the near-infrared region ( $> 800 \text{ nm}$ ), and  $48.41 \text{ mmol}/\text{h}\cdot\text{g}$  under the full Xenon spectrum. This study highlights that rational design of molybdenum-based cocatalyst interfaces holds great promise in developing efficient and sustainable photocatalytic systems for hydrogen production and has potential applications in energy storage and electrochemical devices.

## CRediT authorship contribution statement

Yaoyao Li: Experimental work, writing and data analysis. Chenfang Lou, Wenlin Huang, Ziqiang Ma, Shukai Lin, Xuelian Xie, Tianhao He and Xiaokang Lu: Data curation. Nairong Chen: Data analysis. Jiandong Zhuang: Supervision, writing and data analysis. All authors have given approval to the final version of the manuscript.

## Declaration of Competing Interest

The authors declare that they have no known competing financial



**Scheme 2.** Illustrative diagram of photocatalytic  $\text{H}_2$  evolution mechanism over the MOCS/CdS photocatalyst system under visible-light irradiation.

interests of personal relationships that could have appeared to influence the work reported in this paper.

## Data Availability

No data was used for the research described in the article.

## Acknowledgment

This work is financially supported by Natural Science Foundation of China (No. 22278072), Natural Science Foundation of Fujian Province (No. 2021J01101), Innovation Fund of Fujian Agriculture and Forestry University (No. CXZX2019114S), and National Innovation and Entrepreneurship Training Project for University (No. 202310389014).

## Appendix A. Supporting information

Supplementary data associated with this article can be found in the online version at [doi:10.1016/j.apcatb.2023.123543](https://doi.org/10.1016/j.apcatb.2023.123543).

## References

- [1] S. Cao, L. Piao, X. Chen, Emerging photocatalysts for hydrogen evolution, *Trends Chem.* 2 (2020) 57–70.
- [2] J. Di, C. Yan, A.D. Handoko, Z.W. Seh, H. Li, Z. Liu, Ultrathin two-dimensional materials for photo- and electrocatalytic hydrogen evolution, *Mater. Today* 21 (2018) 749–770.
- [3] R. Li, Latest progress in hydrogen production from solar water splitting via photocatalysis, photoelectrochemical, and photovoltaic-photoelectrochemical solutions, *Chin. J. Catal.* 38 (2017) 5–12.
- [4] C.S. Gopinath, N. Nalajala, A scalable and thin film approach for solar hydrogen generation: a review on enhanced photocatalytic water splitting, *J. Mater. Chem. A* 9 (2021) 1353–1371.
- [5] D. Robert, Photosensitization of TiO<sub>2</sub> by MxOy and MxSy nanoparticles for heterogeneous photocatalysis applications, *Catal. Today* 122 (2007) 20–26.
- [6] X.L. Yin, L.L. Li, W.J. Jiang, Y. Zhang, X. Zhang, L.J. Wan, J.S. Hu, MoS<sub>2</sub>/CdS nanosheets-on-nanorod heterostructure for highly efficient photocatalytic H<sub>2</sub> generation under visible light irradiation, *Acs Appl. Mater. Inter* 8 (2016) 15258–15266.
- [7] K.F. Wu, H.M. Zhu, T.Q. Lian, Ultrafast exciton dynamics and light-driven H<sub>2</sub> evolution in colloidal semiconductor nanorods and Pt-tipped nanorods, *Acc. Chem. Res.* 48 (2015) 851–859.
- [8] Y.-Y. Yang, X.-G. Zhang, C.-G. Niu, H.-P. Feng, P.-Z. Qin, H. Guo, C. Liang, L. Zhang, H.-Y. Liu, L. Li, Dual-channel charges transfer strategy with synergistic effect of Z-scheme heterojunction and LSPR effect for enhanced quasi-full-spectrum photocatalytic bacterial inactivation: new insight into interfacial charge transfer and molecular oxygen activation, *Appl. Catal. B: Environ.* 264 (2020), 118465.
- [9] J. Peng, J. Shen, X. Yu, H. Tang, Zulfiqar, Q. Liu, Construction of LSPR-enhanced 0D/2D CdS/MoO<sub>3</sub> S-scheme heterojunctions for visible-light-driven photocatalytic H<sub>2</sub> evolution, *Chin. J. Catal.* 42 (2021) 87–96.
- [10] F. Gong, M. Liu, S. Ye, L. Gong, G. Zeng, L. Xu, X. Zhang, Y. Zhang, L. Zhou, S. Fang, J. Liu, All-pH stable sandwich-structured MoO<sub>2</sub>/MoS<sub>2</sub>/C hollow nanoreactors for enhanced electrochemical hydrogen evolution, *Adv. Funct. Mater.* 31 (2021) 2101715.
- [11] F. Gao, X. Huang, L. Zhang, Y. Zhao, W. Feng, P. Liu, Crafty design of chemical bonding to construct MoO<sub>2</sub>/CdS nanorod photocatalysts for boosting hydrogen evolution, *Int. J. Hydron. Energy* 44 (2019) 24228–24236.
- [12] S. Zulfiqar, S. Liu, N. Rahman, H. Tang, S. Shah, X.-H. Yu, Q.-Q. Liu, Construction of S-scheme MnO<sub>2</sub>@CdS heterojunction with core-shell structure as H<sub>2</sub>-production photocatalyst, *Rare Met.* 40 (2021) 2381–2391.
- [13] Y. Shi, B. Guo, S.A. Corr, Q. Shi, Y.-S. Hu, K.R. Heier, L. Chen, R. Seshadri, G. D. Stucky, Ordered mesoporous metallic MoO<sub>2</sub> materials with highly reversible lithium storage capacity, *Nano Lett.* 9 (2009) 4215–4220.
- [14] Y. Jin, H. Wang, J. Li, X. Yue, Y. Han, P.K. Shen, Y. Cui, Porous MoO<sub>2</sub> nanosheets as non-noble bifunctional electrocatalysts for overall water splitting, *Adv. Mater.* 28 (2016) 3785–3790.
- [15] B. Guo, X. Fang, B. Li, Y. Shi, C. Ouyang, Y.-S. Hu, Z. Wang, G.D. Stucky, L. Chen, Synthesis and lithium storage mechanism of ultrafine MoO<sub>2</sub> nanorods, *Chem. Mater.* 24 (2012) 457–463.
- [16] Y. Sun, X. Hu, W. Luo, Y. Huang, Self-assembled hierarchical MoO<sub>2</sub>/graphene nanoarchitectures and their application as a high-performance anode material for lithium-ion batteries, *ACS Nano* 5 (2011) 7100–7107.
- [17] Y. Zhang, K. Sun, D. Wu, W. Xie, F. Xie, X. Zhao, X. Wang, Localized surface plasmon resonance enhanced photocatalytic activity via MoO<sub>2</sub>/BiOBr nanohybrids under visible and NIR light, *ChemCatChem* 11 (2019) 2546–2553.
- [18] Q. Zhang, X. Li, W. Yi, W. Li, H. Bai, J. Liu, G. Xi, Plasmonic MoO<sub>2</sub> nanospheres as a highly sensitive and stable non-noble metal substrate for multicomponent surface-enhanced Raman analysis, *Anal. Chem.* 89 (2017) 11765–11771.
- [19] S. Lv, Y. Du, F. Wu, Y. Cai, T. Zhou, Review on LSPR assisted photocatalysis: effects of physical fields and opportunities in multifield decoupling, *Nanoscale Adv.* 4 (2022) 2608–2631.
- [20] W. Wei, Q. Tian, H. Sun, P. Liu, Y. Zheng, M. Fan, J. Zhuang, Efficient visible-light-driven photocatalytic H<sub>2</sub> evolution over MoO<sub>2</sub>-C/CdS ternary heterojunction with unique interfacial microstructures, *Appl. Catal. B: Environ.* 260 (2020), 118153.
- [21] L. Wang, G.-H. Zhang, K.-C. Chou, Study on oxidation mechanism and kinetics of MoO<sub>2</sub> to MoO<sub>3</sub> in air atmosphere, *Int. J. Refract. Met. Hard Mater.* 57 (2016) 115–124.
- [22] J. He, L. Chen, F. Wang, Y. Liu, P. Chen, C.T. Au, S.F. Yin, CdS nanowires decorated with ultrathin MoS<sub>2</sub> nanosheets as an efficient photocatalyst for hydrogen evolution, *ChemSusChem* 9 (2016) 624–630.
- [23] Y. Li, H. Wang, L. Xie, Y. Liang, G. Hong, H. Dai, MoS<sub>2</sub> nanoparticles grown on graphene: an advanced catalyst for the hydrogen evolution reaction, *J. Am. Chem. Soc.* 133 (2011) 7296–7299.
- [24] Y. Yu, S.-Y. Huang, Y. Li, S.N. Steinmann, W. Yang, L. Cao, Layer-dependent electrocatalysis of MoS<sub>2</sub> for hydrogen evolution, *Nano Lett.* 14 (2014) 553–558.
- [25] J. Zhuang, S. Ren, B. Zhu, C. Han, Y. Li, X. Zhang, H. Gao, M. Fan, Q. Tian, Lignin-based carbon dots as high-performance support of Pt single atoms for photocatalytic H<sub>2</sub> evolution, *Chem. Eng. J.* 446 (2022), 136873.
- [26] F. Zeng, M. Yu, W. Cheng, W. He, Y. Pan, Y. Qu, C. Yuan, Tunable surface selenization on MoO<sub>2</sub>-based carbon substrate for notably enhanced sodium-ion storage properties, *Small* 16 (2020), e2001905.
- [27] P. Wang, T. Wu, Y. Ao, C. Wang, Fabrication of noble-metal-free CdS nanorods-carbon layer-cobalt phosphide multiple heterojunctions for efficient and robust photocatalyst hydrogen evolution under visible light irradiation, *Renew. Energy* 131 (2019) 180–186.
- [28] H. Zhang, P. Zhang, M. Qiu, J. Dong, Y. Zhang, X.W. Lou, Ultrasmall MoO<sub>x</sub> clusters as a novel cocatalyst for photocatalytic hydrogen evolution, *Adv. Mater.* 31 (2019) 1804883.
- [29] J. Kibsgaard, Z. Chen, B.N. Reinecke, T.F. Jaramillo, Engineering the surface structure of MoS<sub>2</sub> to preferentially expose active edge sites for electrocatalysis, *Nat. Mater.* 11 (2012) 963–969.
- [30] F. Zeng, H. Liu, Y. Pan, M. Yu, Y. Qu, C. Yuan, Encapsulating N-doped carbon nanorod bundles/MoO<sub>2</sub> nanoparticles via surface growth of ultrathin MoS<sub>2</sub> nanosheets for ultrafast and ultralong cycling sodium storage, *ACS Appl. Mater. Interfaces* 12 (2020) 6205–6216.
- [31] X. Liu, L. Yang, M. Huang, Q. Li, L. Zhao, Y. Sang, X. Zhang, Z. Zhao, H. Liu, W. Zhou, Oxygen vacancy-regulated metallic semiconductor MoO<sub>2</sub> nanobelt photoelectron and hot electron self-coupling for photocatalytic CO<sub>2</sub> reduction in pure water, *Appl. Catal. B: Environ.* 319 (2022), 121887.
- [32] L.M. Malard, M.A. Pimenta, G. Dresselhaus, M.S. Dresselhaus, Raman spectroscopy in graphene, *Phys. Rep.* 473 (2009) 51–87.
- [33] J. Liu, P. Wang, L. Gao, X. Wang, H. Yu, In situ sulfuration synthesis of heterostructure MoS<sub>2</sub>-Mo<sub>2</sub>C@C for boosting the photocatalytic H<sub>2</sub> production activity of TiO<sub>2</sub>, *J. Mater. Chem. C* 10 (2022) 3121–3128.
- [34] M. Dieterle, G. Mestl, Raman spectroscopy of molybdenum oxides Part II. Resonance Raman spectroscopic characterization of the molybdenum oxides Mo<sub>4</sub>O<sub>11</sub> and Mo<sub>2</sub>O<sub>5</sub>, *Phys. Chem. Chem. Phys.* 4 (2002) 822–826.
- [35] F. Xing, H. Yu, C. Cheng, Q. Liu, L. Lai, S. Xia, C. Huang, Interfacial microenvironment-regulated cascade charge transport in Co<sub>6</sub>Mo<sub>6</sub>C<sub>2</sub>-MoO<sub>2</sub>-CoNC@ZnIn<sub>2</sub>S<sub>4</sub> photocatalyst for efficient hydrogen evolution, *Chem. Eng. J.* 450 (2022), 138130.
- [36] M. Placidi, M. Dimitrijevska, V. Izquierdo-Roca, X. Fontané, A. Castellanos-Gomez, A. Pérez-Tomás, N. Mestres, M. Espindola-Rodríguez, S. López-Marino, M. Neuschitzer, V. Bermudez, A. Yaremko, A. Pérez-Rodríguez, Multiwavelength excitation Raman scattering analysis of bulk and two-dimensional MoS<sub>2</sub>: vibrational properties of atomically thin MoS<sub>2</sub> layers, *2D Mater.* 2 (2015), 035006.
- [37] H. Li, Q. Zhang, C.C.R. Yap, B.K. Tay, T.H.T. Edwin, A. Olivier, D. Baillargeat, From bulk to monolayer MoS<sub>2</sub>: evolution of raman scattering, *Adv. Funct. Mater.* 22 (2012) 1385–1390.
- [38] M. Zoller, R. Bubnova, Y. Biryukov, E. Haussühl, R. Pöttgen, O. Janka, S. Penner, C. Praty, H. Fitzek, J. Winkler, S. Filatov, H. Huppertz, Elucidating the physical properties of the molybdenum oxide Mo<sub>4</sub>O<sub>11</sub> and its tantalum substituted variant Mo<sub>2</sub>Ta<sub>2011</sub>, *Z. für Krist. - Cryst. Mater.* 235 (2020) 143–155.
- [39] Z.Y. Liu, P.F. Shan, K.Y. Chen, M. Marshall, S. Zhang, T. Yong, H.S. Deng, X. Yin, Y. Ding, H.M. Weng, Y. Uwatoko, P. Dera, W. Xie, Y. Sui, J.G. Cheng, High-pressure insulating phase of Mo<sub>4</sub>O<sub>11</sub> with collapsed volume, *Phys. Rev. B* 104 (2021), 024105.
- [40] M. Dieterle, G. Weinberg, G. Mestl, Raman spectroscopy of molybdenum oxides, *Phys. Chem. Chem. Phys.* 4 (2002) 812–821.
- [41] M. Dieterle, G. Mestl, Raman spectroscopy of molybdenum oxides, *Phys. Chem. Chem. Phys.* 4 (2002) 822–826.
- [42] P. Saha, A.J. Anderson, T. Lee, M. Klemm, The solubility of tugarinovite (MoO<sub>2</sub>) in H<sub>2</sub>O at elevated temperatures and pressures, *Geofluids* 2017 (2017) 1–12.
- [43] F. Gao, Y. Zhao, L. Zhang, B. Wang, Y. Wang, X. Huang, K. Wang, W. Feng, P. Liu, Well dispersed MoC quantum dots in ultrathin carbon films as efficient co-catalysts for photocatalytic H<sub>2</sub> evolution, *J. Mater. Chem. A* 6 (2018) 18979–18986.
- [44] H. Lin, Z. Shi, S. He, X. Yu, S. Wang, Q. Gao, Y. Tang, Heteronanowires of MoC-Mo<sub>2</sub>C as efficient electrocatalysts for hydrogen evolution reaction, *Chem. Sci.* 7 (2016) 3399–3405.
- [45] C. Wan, Y.N. Regmi, B.M. Leonard, Multiple phases of molybdenum carbide as electrocatalysts for the hydrogen evolution reaction, *Angew. Chem. Int. Ed. Engl.* 53 (2014) 6407–6410.

[46] M.A. Camacho-López, L. Escobar-Alarcón, M. Picquart, R. Arroyo, G. Córdoba, E. Haro-Poniatowski, Micro-Raman study of the m-MoO<sub>2</sub> to  $\alpha$ -MoO<sub>3</sub> transformation induced by cw-laser irradiation, *Opt. Mater.* 33 (2011) 480–484.

[47] H. Zhang, P. Zhang, M. Qiu, J. Dong, Y. Zhang, X.W. Lou, Ultrasmall MoO<sub>x</sub> clusters as a novel cocatalyst for photocatalytic hydrogen evolution, *Adv. Mater.* (2018), 1804883.

[48] H. Cao, X. Hu, W. Shi, S. Li, Y. Huang, pH-regulated reversible photoluminescence and localized surface plasmon resonances arising from molybdenum oxide quantum dot, *Appl. Mater. Today* 18 (2020), 100516.

[49] S. Qiu, Y. Shen, G. Wei, S. Yao, W. Xi, M. Shu, R. Si, M. Zhang, J. Zhu, C. An, Carbon dots decorated ultrathin CdS nanosheets enabling in-situ anchored Pt single atoms: a highly efficient solar-driven photocatalyst for hydrogen evolution, *Appl. Catal. B: Environ.* (259) (2019).

[50] C. Cheng, B. He, J. Fan, B. Cheng, S. Cao, J. Yu, An inorganic/organic S-scheme heterojunction H(2) -production photocatalyst and its charge transfer mechanism, *Adv. Mater.* 33 (2021), e2100317.

[51] X. Chang, T. Wang, P. Zhang, J. Zhang, A. Li, J. Gong, Enhanced surface reaction kinetics and charge separation of p-n heterojunction Co<sub>3</sub>O<sub>4</sub>/BiVO<sub>4</sub> photoanodes, *J. Am. Chem. Soc.* 137 (2015) 8356–8359.

[52] X. Xue, W. Dong, Q. Luan, H. Gao, G. Wang, Novel interfacial lateral electron migration pathway formed by constructing metallized CoP<sub>2</sub>/CdS interface for excellent photocatalytic hydrogen production, *Appl. Catal. B: Environ.* 334 (2023), 122860.